Autonomous Actuation of Zero Modes in Mechanical Networks Far from Equilibrium

Francis G. Woodhouse,[1,*] Henrik Ronellenfitsch,[2] and Jörn Dunkel[2]
[1]Department of Applied Mathematics and Theoretical Physics, Centre for Mathematical Sciences, University of Cambridge, Wilberforce Road, Cambridge CB3 0WA, United Kingdom
[2]Department of Mathematics, Massachusetts Institute of Technology, 77 Massachusetts Avenue, Cambridge, Massachusetts 02139-4307, USA

(Received 21 June 2018; revised manuscript received 4 September 2018; published 23 October 2018)

A zero mode, or floppy mode, is a nontrivial coupling of mechanical components yielding a degree of freedom with no resistance to deformation. Engineered zero modes have the potential to act as microscopic motors or memory devices, but this requires an internal actuation mechanism that can overcome unwanted fluctuations in other modes and the dissipation inherent in real systems. In this Letter, we show theoretically and experimentally that complex zero modes in mechanical networks can be selectively mobilized by nonequilibrium activity. We find that a correlated active bath actuates an infinitesimal zero mode while simultaneously suppressing fluctuations in higher modes compared to thermal fluctuations, which we experimentally mimic by high frequency shaking of a physical network. Furthermore, self-propulsive dynamics spontaneously mobilize finite mechanisms as exemplified by a self-propelled topological soliton. Nonequilibrium activity thus enables autonomous actuation of coordinated mechanisms engineered through network topology.

DOI: 10.1103/PhysRevLett.121.178001

Soft, electronics-free assemblies capable of autonomous motion and reconfiguration are emerging as the basis of new adaptable smart materials. Macroscopic morphology schemes, such as snap through [1–5] and buckling [6–8] driven by heat [9] or chemo-fluidics [10], are complemented by the robustness of topological modes [11–15] to give a wide set of components based on elastic networks [16–20]. In such networks, a zero mode (ZM) arises as a degree of freedom with no resistance to small deformation, either as an infinitesimal zero mode (IZM) with resistance at a nonlinear order [21–29] or a mechanism with a continuous range of motion [25–27,30,31]. A designed ZM can potentially be exploited as a complex coupling [32,33] in an internally driven material. However, actuation of a ZM can be hampered by indiscriminate simultaneous excitation of nonzero harmonic modes (HMs), particularly in noisy microscopic systems [29,34–38]. Nonequilibrium processes [39], which support intricate topological edge currents [40–42] and unorthodox stress responses [43,44], may hold the key to overcoming this actuation dilemma.

In this Letter, we show that active matter provides effective schemes to autonomously actuate a mechanical ZM. Active biophysical systems, such as bacterial suspensions or self-propelled microswimmers, convert disperse environmental energy into directed motion [45–47]. Tracers in an active bath, and the active particles themselves, then have positional statistics differing from thermal white noise [48–50]. This statistical "color," which depends on properties such as fuel availability and suspension density, can be used to drive mode actuation statistics away from equilibrium in a controllable fashion [51,52], meaning features such as geometric asymmetry can be exploited to do work [53,54]. First, we show that correlated noise generated by an active matter bath [49] can actuate a complex mechanical IZM while markedly suppressing HMs to a degree dependent on temporal correlations, as well as exemplifying experimentally that fluctuation-based IZM actuation can be mimicked by simple high-frequency shaking. We then broaden to self-propulsive Rayleigh activity [55–57], appropriate for a network whose nodes have intrinsic motility [58]. We show that this scheme mobilizes a full mechanism comprising a propagating domain boundary in the SSH lattice [11,27], suggesting that Goldstone modes of arbitrary complex systems can be mobilized by nonequilibrium driving [51,59,60].

To gain intuition about the core idea, consider this basic example: a mass is held between two fixed points, $\hat{\boldsymbol{x}} = (1, 0)$ and $-\hat{\boldsymbol{x}}$, in the plane by two identical springs of unit natural length and stiffness [Fig. 1(a)] [38]. Let $\boldsymbol{x} = (x, y)$ be the offset of the mass from its equilibrium (0,0). The total elastic potential energy is

$$H(\boldsymbol{x}) = \frac{1}{2}[(|\boldsymbol{x} - \hat{\boldsymbol{x}}| - 1)^2 + (|\boldsymbol{x} + \hat{\boldsymbol{x}}| - 1)^2]. \qquad (1)$$

If the mass is excited by thermal noise of temperature T, its position is Boltzmann distributed with $p(\boldsymbol{x}) \propto e^{-H/T}$. To leading order in $T \ll 1$, p can be approximated by $p_0(\boldsymbol{x}) \propto e^{-H_0/T}$ where $H_0 = x^2 + \frac{1}{4}y^4$ [38]. This bare Hamiltonian shows the two eigenmodes: an HM of frequency $\sqrt{2}$

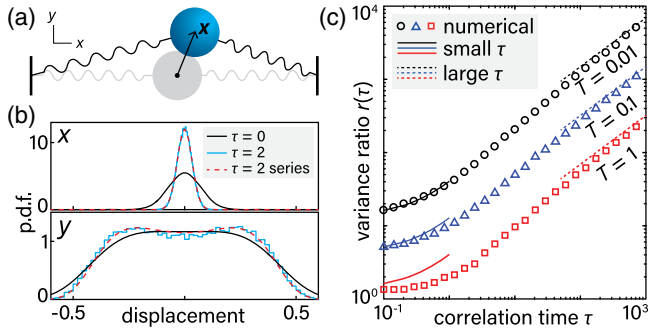

FIG. 1. Zero mode actuation in a bead–spring model. (a) Single mass at offset (x, y), with HM in x and IZM in y [38]. (b) Comparison of $T = 0.01$ exact marginal densities of x and y at $\tau = 0$ (black) with $\tau = 2$ densities from simulation (blue) and approximated from Eqs. (1) and (2) (red dashed). Histogram for $\tau = 2$ from 50 000 samples, others by quadrature (Supplemental Material [61]). (c) Variance ratio $r(\tau) = \langle y^2\rangle/\langle x^2\rangle$ from simulations (markers) with approximations for small τ (solid lines) and large τ (dashed lines) from Eqs. (3) and (4): 5000 samples per marker; 95% CIs smaller than markers (Supplemental Material [61]).

parallel to the springs, and an IZM perpendicular to the springs. Scaling considerations then imply that the variances $\langle x^2\rangle$ and $\langle y^2\rangle$ vary as T and $\sqrt{T}$, respectively. The fine details can be seen by formal expansion in $\sqrt{T}$ (Supplemental Material [61]), in which interaction cross terms are negligible as $T \to 0$; this does not hold in the more complex examples below, where broken symmetries induce non-negligible interactions $\propto xy^2$ in H_0 that can cause strong violation of naive equipartition $\langle x^2\rangle \sim T/\omega^2$. Either way, the basic T-scalings still hold, so $\langle y^2\rangle/\langle x^2\rangle \to \infty$ as $T \to 0$. Thus fluctuations in the IZM dominate those in the HM at a low temperature.

Uncorrelated noise is a crude tool, with only one control parameter. Actuation by biological or chemical active matter [58,66] can allow finer tuning. The forces generated by a motile bath can be modelled by an Ornstein–Uhlenbeck process $\boldsymbol{\xi}$ obeying $\tau\dot{\boldsymbol{\xi}} = -\boldsymbol{\xi} + \boldsymbol{\eta}$, where $\boldsymbol{\eta}$ is a thermal process with variance $2\gamma T$ for amplitude T and friction γ, and τ is the correlation time [50,67]. These parameters depend on the properties of the active medium [49], and so by changing these properties—density, temperature, fuel concentration—the statistics can be tuned. In the overdamped limit with γ rescaled to one, it was shown in Ref. [50] that small $\tau \ll 1$ adjusts H to an effective potential

$$H_{\text{eff}} = H + \tau\left[\frac{1}{2}|\boldsymbol{\nabla}H|^2 - T\nabla^2 H\right] + O(\tau^2). \tag{2}$$

For our example in Fig. 1, this (or the unified colored noise approximation [68,69]) gives a low-T expansion $H_{\text{eff}} = (1 + 2\tau)x^2 + \frac{1}{4}y^4 + \cdots$, implying

$$\frac{\langle y^2\rangle}{\langle x^2\rangle} \approx \frac{4\Gamma(\frac{3}{4})}{\Gamma(\frac{1}{4})}\frac{1 + 2\tau}{\sqrt{T}} \tag{3}$$

for small T and τ {Supplemental Material [61]; Fig. 1(c)}. This is reflected in the $\tau = 2$ marginal densities [Fig. 1(b)]: x contracts, while y is unchanged except for a small bimodality directly analogous to boundary accumulation of microswimmers [70]. In the opposite limit $\tau \gg 1$, where Eq. (2) does not hold, we show in the Supplemental Material [61] that separation of time scales gives the asymptotic power law

$$\frac{\langle y^2\rangle}{\langle x^2\rangle} \approx \frac{2^{7/3}\Gamma(\frac{5}{6})}{\pi^{1/2}}\left(\frac{\tau}{T}\right)^{2/3}, \tag{4}$$

as τ/T grows large [Fig. 1(c)]. These results demonstrate that active noise is an effective means to actuate an IZM.

In a general mechanical network, the same ideas can be used to actuate an IZM with many masses moving in a complex, coordinated fashion. A stable mechanical network comprises nodes α with rest positions $\boldsymbol{x}_\alpha^0$, and Hookean elastic bonds (α, β) between nodes α and β of natural lengths $\ell_{\alpha\beta} = |\boldsymbol{x}_\alpha^0 - \boldsymbol{x}_\beta^0|$ and stiffnesses $k_{\alpha\beta} > 0$. When the nodes are perturbed to $\boldsymbol{x}_\alpha$ the network has elastic energy

$$H(\{\boldsymbol{x}_\alpha\}) = \frac{1}{2}\sum_{(\alpha,\beta)} k_{\alpha\beta}(|\boldsymbol{x}_\alpha - \boldsymbol{x}_\beta| - \ell_{\alpha\beta})^2,$$

which is minimized if (but not always only if) $\boldsymbol{x}_\alpha = \boldsymbol{x}_\alpha^0$. Node α then feels an elastic force $\boldsymbol{F}_\alpha = -\boldsymbol{\nabla}_\alpha H$, where we notate $\boldsymbol{\nabla}_\alpha \equiv \partial/\partial\boldsymbol{x}_\alpha$. Large real-world systems also possess dissipation, which we include as a linear friction force $\gamma\dot{\boldsymbol{x}}_\alpha$. In general, dissipation within bonds [1] could also be included as forces $\propto \dot{\boldsymbol{x}}_\alpha - \dot{\boldsymbol{x}}_\beta$ giving a nondiagonal friction matrix [71]. We further restrict to two dimensions, and assume all nodes are identical, adopting units in which node masses are one and other constants are scaled by a characteristic stiffness and length (Supplemental Material [61]). Finally, we pin boundary nodes (Figs. 2 and 3) or particular interior nodes (Fig. 4) to eliminate rigid body translations and rotation.

Without any actuation, the mobile nodes obey passive force balance, namely $\ddot{\boldsymbol{x}}_\alpha = -\boldsymbol{\nabla}_\alpha H - \gamma\dot{\boldsymbol{x}}_\alpha$. Consider a small perturbation $\boldsymbol{x}_\alpha = \boldsymbol{x}_\alpha^0 + \boldsymbol{\epsilon}_\alpha$ of the rest state, and let $\boldsymbol{e}$ be the vector obtained by flattening $\boldsymbol{\epsilon}_\alpha$. To first order, $\boldsymbol{e}$ obeys $\ddot{e}_i = -\sum_j D_{ij}e_j - \gamma\dot{e}_i$, where the Hessian $D_{ij} = \partial_i\partial_j H(\boldsymbol{x}^0)$ is the dynamical matrix [11]. The orthonormal eigenvectors $\{\boldsymbol{v}_k\}$ of D_{ij} give the fundamental modes of the elastic network, whose non-negative eigenvalues $\{\omega_k^2\}$ determine if each mode is an HM ($\omega_k^2 > 0$) or a ZM ($\omega_k^2 = 0$). These then form a basis for configurations $\boldsymbol{x}_\alpha$. Writing $c_k(t)$ for the component of mode k at time t, given by dotting the flattened $\boldsymbol{x}_\alpha(t)$ with $\boldsymbol{v}_k$, we define the

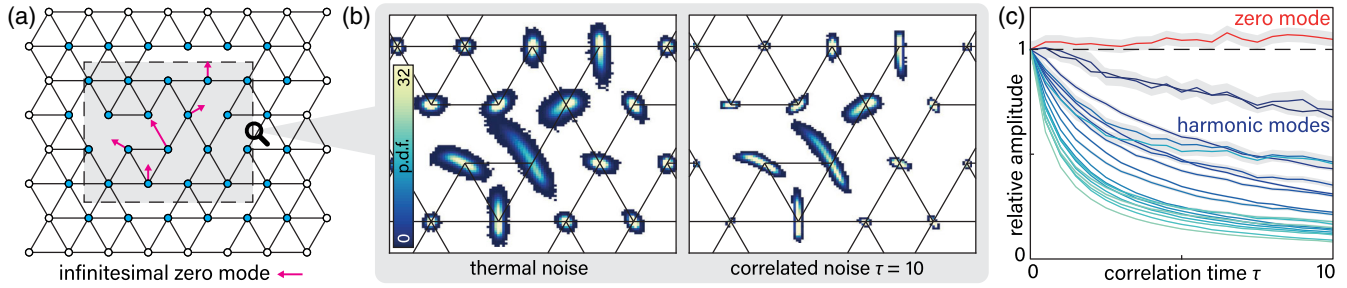

FIG. 2. Active noise actuates an IZM while suppressing HMs in a mechanical network (Supplemental Material Videos 1 and 2 [61]). (a) A network of unit length, unit stiffness springs is designed to contain exactly one IZM (arrows). White nodes are pinned. (b) Histograms of node positions in highlighted area of (a) when actuated by thermal noise (left) and correlated noise with $\tau = 10$ (right) of strength $T = 10^{-3}$. The IZM is more cleanly actuated by correlated noise while HMs are suppressed. (c) Thermal-relative amplitude $\langle u_i^2\rangle_\tau/\langle u_i^2\rangle_{\tau=0}$ of the 21 lowest eigenvalue modes u_i of (a) from numerical integration at $0 \le \tau \le 10$, with $T = 10^{-3}$ fixed to maintain constant intensity $\overline{\langle v_{\alpha i}(0) v_{\beta j}(t)\rangle}$. The IZM (red) is barely affected, while HMs (blues) diminish. Grey areas are estimated 95% CIs; data from 20 realizations to $t = 2 \times 10^4$ with $\delta t = 10^{-4}$ at each of 20 values of τ (Supplemental Material [61]).

amplitude of mode k to be the time average of its squared coefficient, $\langle c_k(t)^2\rangle$. Our goal is to show that the amplitudes of ZMs can be selectively actuated in suitably designed networks.

When a network is actuated by active forces on its nodes, its dynamics depends on both its structure and the type of activity. The positions $\boldsymbol{x}_\alpha$ obey the general actuated dynamics

$$\ddot{\boldsymbol{x}}_\alpha = -\boldsymbol{\nabla}_\alpha H - \gamma \dot{\boldsymbol{x}}_\alpha + \boldsymbol{F}_\alpha(\dot{\boldsymbol{x}}_\alpha; t), \tag{5}$$

where $\boldsymbol{F}_\alpha$ represents the actuation process. For this process we will consider not only the thermal and correlated active bath processes exemplified above, but also strong self-propulsive activity through internal energy depot actuation. These incorporate increasing levels of nonequilibrium dynamics, which progressively actuate infinitesimal and finite zero modes.

Generalizing the single mass example above, a mechanical network driven by Ornstein-Uhlenbeck noise can be formulated with an extra vector $\boldsymbol{\xi}_\alpha$ for each node [50,70,72]. These follow

$$\tau \dot{\boldsymbol{\xi}}_\alpha = -\boldsymbol{\xi}_\alpha + \boldsymbol{\eta}_\alpha \tag{6}$$

for independent Gaussian noise processes $\{\eta_{\alpha i}\}$ of variances $2\gamma T$. We set $\boldsymbol{F}_\alpha = \boldsymbol{\xi}_\alpha$, giving actuation forces correlated as $\langle \xi_{\alpha i}(t)\xi_{\beta j}(t')\rangle = \delta_{\alpha\beta}\delta_{ij}(\gamma T/\tau)e^{-|t-t'|/\tau}$. The limit $\tau \to 0$ then gives thermal noise. We also again take the overdamped limit, appropriate for immersion in an active matter bath. After rescaling to set γ to 1, this gives first-order dynamics

$$\dot{\boldsymbol{x}}_\alpha = -\boldsymbol{\nabla}_\alpha H + \boldsymbol{\xi}_\alpha, \tag{7}$$

which are subject to Eq. (6). Varying τ while holding T fixed then probes the effect of increasing activity-driven correlations at constant actuation intensity $\overline{\langle \xi_{\alpha i}(0)\xi_{\beta j}(t)\rangle}$.

For a mechanical network designed to have a nontrivial isolated IZM {Fig. 2(a); Supplemental Material [61]}, correlated noise highlights the IZM and suppresses fluctuations at other nodes. Numerical integration of Eq. (7) shows that, while thermal noise ($\tau = 0$) actuates the IZM with significant surrounding fluctuations {Fig. 2(b); Supplemental Material Video 1 [61]}, an active process with $\tau > 0$ damps HM fluctuations relative to those of the IZM {Fig. 2(b); Supplemental Material Video 2 [61]}. This is confirmed in the mode amplitudes $\langle c_k^2\rangle$, shown in Fig. 2(c): the IZM amplitude remains at its $\tau = 0$ level, while HMs decay as τ increases. Two further examples showing IZM preservation and HM suppression are given in the Supplemental Material [61]. The same suppression is not guaranteed if the ZM contains a low-coordination node with bistability in its position (Supplemental Material [61]), since the fluctuation basis depends on the state of the bistable node, but this can typically be avoided in design.

Even without correlation, persistent low-temperature ZM-HM coupling enhances mode amplitudes and causes naïve equipartition to fail. In a system comprising only HMs u_i of frequencies ω_i, two-mode interactions are diagonalized away and the lowest-order terms remaining are at best third order. For low temperatures $T \ll 1$, interactions can thus be neglected relative to harmonic energies u_i^2 and simple equipartition of independent modes $\langle u_i^2\rangle \approx T/\omega_i^2$ is a good amplitude estimate. However, with a quartic ZM v present, there are three types of lowest-order term in $T \ll 1$: the independent mode energies v^4 and u_i^2, and ZM-HM interactions $u_i v^2$. Interactions contribute an effective repulsive quartic potential on the ZM, causing its amplitude $\langle v^2\rangle$ to increase with every additional HM interaction (Supplemental Material [61]). Moreover, the HM amplitudes $\langle u_i^2\rangle$ are also increased by their interactions with the ZM (Supplemental Material [61]).

Small- and large-τ asymptotics provide general principles for the behavior of network modes. When $\tau \ll 1$,

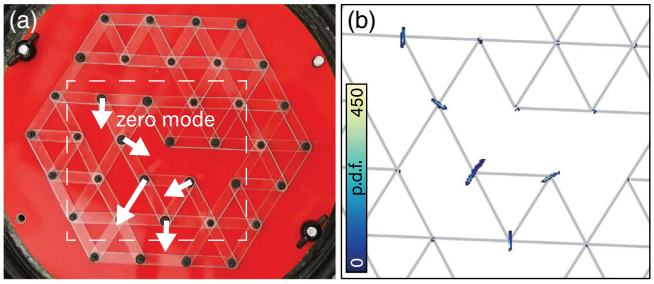

FIG. 3. Shaking actuates the IZM of a stiff mechanical network (Supplemental Material Video 3 [61]). (a) Photograph of network with isolated IZM (arrows) constructed from plastic. Joints are freely rotating pins, with boundary nodes fixed in position. (b) Actuating the network by high frequency shaking mobilizes the IZM, shown by node positional histograms for the subregion indicated in (a) computed by particle tracking over 14 min with distances rescaled by mean edge length. (See Supplemental Material [61] for experimental methods.)

computing the effective potential in Eq. (2) [50] for an arbitrary small-T expansion $H \approx \sum_i a_i u_i^2 + \sum_i b_i u_i v^2 + Av^4$ in HMs u_i and a quartic IZM v gives new effective coefficients incorporating τ to leading order (Supplemental Material [61]). In particular, the stiffnesses a_i become $a_i(1 + 2\tau a_i)$, showing that weaker modes have a proportionally weaker response to increasing τ, while $\langle v^2 \rangle$ is unchanged. Conversely, as $\tau \to \infty$, a scaling analysis shows that an IZM has amplitude proportional to $(T/\tau)^{1/3}$ while all HMs have amplitude proportional to (T/τ) (Supplemental Material [61]), generalizing our earlier example. Physical dependencies are clarified by restoring dimensionful parameters, turning T/τ into $\gamma T/\kappa^2 \lambda^2 \tau$ for typical spring stiffness κ and length λ.

In a real mechanical network, local activity can be mimicked by the randomization generated through high frequency shaking. We fabricated a stiff-edged network designed to contain an isolated IZM [Fig. 3(a)] by connecting plastic edges with freely rotating joints. We then actuated the network by mounting it on a baseboard, with fixed edge nodes, and securing this board to a loudspeaker (Supplemental Material [61]). The speaker was driven at 49 Hz with 20% Ornstein-Uhlenbeck noise of correlation time $(1/345)$ s to prevent metastable sticking (Supplemental Material [61]). The baseboard collisions generated by the high-frequency shaking randomizes the motion of the IZM, actuating it through motion allowed by slight pliability in the pin joints {Fig. 3(b) and Supplemental Material Video 3 [61]}. The effective activity, and so the relative actuation of the IZM and HMs, can be controlled by changing the actuation frequency (Supplemental Material [61]). Thus even elementary actuation strategies can be of practical use for IZM mobilization.

We now turn to a stronger form of activity. If the masses themselves are motile, able to convert chemical energy to kinetic energy, an effective model is to introduce what amounts to a negative frictional response at low speeds [56,57]. Appealing to expansion techniques, as in the Toner-Tu model [73], we use simple Rayleigh activity [71] with a velocity-dependent propulsive force

$$\boldsymbol{F}_\alpha = \gamma_f(1 - |\dot{\boldsymbol{x}}_\alpha|^2/v^2)\dot{\boldsymbol{x}}_\alpha, \tag{8}$$

where γ_f sets the force strength and v is a natural speed in the absence of friction. The overall effective friction force can then be viewed as $\gamma\dot{\boldsymbol{x}}_\alpha - \boldsymbol{F}_\alpha \equiv f(|\dot{\boldsymbol{x}}_\alpha|)\dot{\boldsymbol{x}}_\alpha$ with effective friction coefficient $f(u) = \gamma - \gamma_f + \gamma_f u^2/v^2$. Provided that $\gamma_0 \equiv \gamma - \gamma_f < 0$, this gives a natural speed $v_0 = v|\gamma_0/\gamma_f|^{1/2}$ below which $f(u) < 0$. The quiescent state is then rendered unstable: to linear order, a perturbation of any eigenmode grows at least as fast as $e^{|\gamma_0/2|t}$ (Supplemental Material [61]). Nonlinear effects bound this growth, giving oscillatory trajectories for constrained systems [56].

Under Rayleigh actuation, deviations in the ZM dominate those in the HM at small v_0, as for correlated noise, with extra oscillatory structure in time. Take once more the example in Fig. 1. At small γ_0, the leading order behavior is a conservative oscillator $\ddot{\boldsymbol{x}} = -\boldsymbol{\nabla}H$ whose amplitude

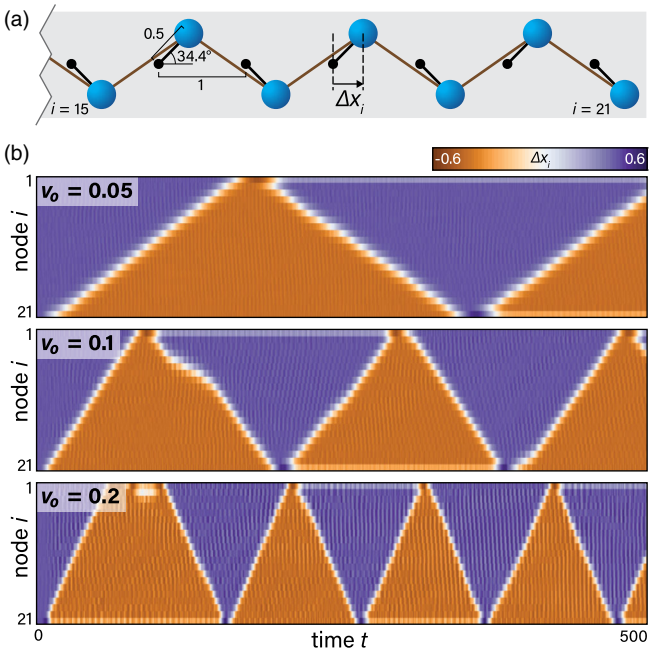

FIG. 4. Self-propulsive activity spontaneously mobilizes a complex mechanism (Supplemental Material Video 5 [61]). (a) Mechanical SSH model [11,27], which has a periodic mechanism comprising progressive flipping of the masses from right to left and back again. Black nodes are fixed, blue nodes are mobile. (b) Endowing a 21-node chain with self-propulsive activity spontaneously mobilizes the mechanism. The progression speed depends on the propulsion v_0, seen through the time-dependent offsets Δx_i of mobile nodes from their pinning points. All bonds of strength $k = 10$ with $\gamma_0 = 1$, integrated at $\delta t = 10^{-5}$ from initial random perturbation.

is set by kinetic-to-potential energy balance $v_0^2 \sim H$ (Supplemental Material [61]). The ZM-HM variance ratio therefore scales as $\langle y^2 \rangle / \langle x^2 \rangle \sim 1/v_0$, which diverges as $v_0 \to 0$. A similar divergence occurs in the "overdamped" case $\gamma_0 \gg 1$. This same suppression of HMs persists in more complex networks (Supplemental Material [61]; Supplemental Material Video 4 [61]).

Beyond IZMs, self-propulsion distinguishes itself from an active bath in its ability to fully mobilize free-moving mechanisms [36] even in topologically complex cases. For a node tethered to just one fixed point, invariance means that the dynamics of the rotation angle θ has no elastic term. The node therefore accelerates and sustains an angular velocity $\sim v_0$ in the finite mechanism. This principle generalizes to intricate mechanisms of large mechanical networks. Recently, a mechanical chain inspired by the SSH model of polyacetylene [Fig. 4(a)] has emerged as a rich source of topological phenomena [11,27]. This chain possesses a ZM localized at the boundary [11], which gives rise to a finite mechanism manifesting as a domain boundary propagating along the chain [27]. Ordinarily, to begin propagating an external energy input is needed, either by a manual "kick" of the end nodes or by a global force field. But persistent propagation is difficult: motion by a "kick" will inevitably slow and stop due to dissipation, while an external field needs regular adjustment to keep the defect moving between the two ends of the finite chain. Endowing each node with active propulsion spontaneously actuates the ZM, mobilizing the boundary and causing a domain wall soliton to propagate autonomously along the chain {Fig. 4(b); Supplemental Material Video 5 [61]}. While under passive dynamics the propagation speed of the topological soliton is set by the initial kinetic energy or the external force strength, here this is controlled by v_0, the effective self-propulsive speed [Fig. 4(b)]. The defect can propagate cleanly for multiple cycles up and down the chain, with occasional stalls or reversals caused by the complex interactions of the fluctuating active nodes (Supplemental Material [61]).

To conclude, we have shown that both nonequilibrium active baths and intrinsic self-propulsion can actuate infinitesimal and finite zero modes of mechanical networks. Rapid progress in developing artificial active systems [58,66] suggests practical routes to engineer active mechanical networks exhibiting fine-tuned fluctuation spectra or even complex response phenomena, such as nonreciprocity [23,74] enabled by asymmetric nonlinear zero modes and nonequilibrium steady state statistics. These networks could be used to perform complex mechanical tasks, such as enhancing transport of transiently bound colloids, or to extract work from an active medium [59] by attaching magnetic beads to drive a miniature dynamo, for example. In general, we expect that any Goldstone mode of a complex mechanical system can be selectively mobilized by nonequilibrium activity of this kind [51].

We thank Pedro Sáenz for assistance with the experimental setup, and Ellen A. Donnelly and Martin Zwierlein for helpful discussions. This work was supported by Trinity College, Cambridge (F. G. W.), a GPU donation from NVIDIA Corporation (F. G. W.), an Edmund F. Kelly Research Award (J. D.), an MIT Solomon Buchsbaum Research Fund Award (J. D.), and a James S. McDonnell Foundation Complex Systems Scholar Award (J. D.).

*Present address: Mathematical Institute, University of Oxford, Andrew Wiles Building, Radcliffe Observatory Quarter, Woodstock Road, Oxford OX2 6GG, United Kingdom.
Corresponding author.
francis.woodhouse@maths.ox.ac.uk

[1] J. R. Raney, N. Nadkarni, C. Daraio, D. M. Kochmann, J. A. Lewis, and K. Bertoldi, Proc. Natl. Acad. Sci. U.S.A. **113**, 9722 (2016).
[2] M. Gomez, D. E. Moulton, and D. Vella, Nat. Phys. **13**, 142 (2017).
[3] M. Gomez, D. E. Moulton, and D. Vella, Phys. Rev. Lett. **119**, 144502 (2017).
[4] T. Chen, O. R. Bilal, K. Shea, and C. Daraio, arXiv: 1710.04723.
[5] J. T. B. Overvelde, T. Kloek, J. J. A. D'haen, and K. Bertoldi, Proc. Natl. Acad. Sci. U.S.A. **112**, 10863 (2015).
[6] H. Fu *et al.*, Nat. Mater. **17**, 268 (2018).
[7] C. Baek, A. O. Sageman-Furnas, M. K. Jawed, and P. M. Reis, Proc. Natl. Acad. Sci. U.S.A. **115**, 75 (2018).
[8] S. H. Kang, S. Shan, A. Košmrlj, W. L. Noorduin, S. Shian, J. C. Weaver, D. R. Clarke, and K. Bertoldi, Phys. Rev. Lett. **112**, 098701 (2014).
[9] Z. Ding, C. Yuan, X. Peng, T. Wang, H. J. Qi, and M. L. Dunn, Sci. Adv. **3**, e1602890 (2017).
[10] M. Wehner, R. L. Truby, D. J. Fitzgerald, B. Mosadegh, G. M. Whitesides, J. A. Lewis, and R. J. Wood, Nature (London) **536**, 451 (2016).
[11] C. L. Kane and T. C. Lubensky, Nat. Phys. **10**, 39 (2014).
[12] T. C. Lubensky, C. L. Kane, X. Mao, A. Souslov, and K. Sun, Rep. Prog. Phys. **78**, 073901 (2015).
[13] D. Zhou, L. Zhang, and X. Mao, Phys. Rev. Lett. **120**, 068003 (2018).
[14] B. G. -g. Chen, B. Liu, A. A. Evans, J. Paulose, I. Cohen, V. Vitelli, and C. Santangelo, Phys. Rev. Lett. **116**, 135501 (2016).
[15] R. Süsstrunk and S. D. Huber, Science **349**, 47 (2015).
[16] K. Bertoldi, V. Vitelli, J. Christensen, and M. van Hecke, Nat. Rev. Mater. **2**, 17066 (2017).
[17] J. L. Silverberg, A. A. Evans, L. McLeod, R. C. Hayward, T. Hull, C. D. Santangelo, and I. Cohen, Science **345**, 647 (2014).
[18] J. T. B. Overvelde, J. C. Weaver, C. Hoberman, and K. Bertoldi, Nature (London) **541**, 347 (2017).
[19] N. Yang and J. L. Silverberg, Proc. Natl. Acad. Sci. U.S.A. **114**, 3590 (2017).
[20] C. Coulais, E. Teomy, K. de Reus, Y. Shokef, and M. van Hecke, Nature (London) **535**, 529 (2016).
[21] C. R. Calladine and S. Pellegrino, Int. J. Solids Struct. **27**, 505 (1991).

[22] C. Heussinger and E. Frey, Phys. Rev. Lett. **97**, 105501 (2006).
[23] C. Coulais, D. Sounas, and A. Alù, Nature (London) **542**, 461 (2017).
[24] X. Mao, N. Xu, and T. C. Lubensky, Phys. Rev. Lett. **104**, 085504 (2010).
[25] K. Sun, A. Souslov, X. Mao, and T. C. Lubensky, Proc. Natl. Acad. Sci. U.S.A. **109**, 12369 (2012).
[26] S. D. Guest and J. W. Hutchinson, J. Mech. Phys. Solids **51**, 383 (2003).
[27] B. G. Chen, N. Upadhyaya, and V. Vitelli, Proc. Natl. Acad. Sci. U.S.A. **111**, 13004 (2014).
[28] J. Paulose, B. G. Chen, and V. Vitelli, Nat. Phys. **11**, 153 (2015).
[29] K. Chen, W. G. Ellenbroek, Z. Zhang, D. T. N. Chen, P. J. Yunker, S. Henkes, C. Brito, O. Dauchot, W. Van Saarloos, A. J. Liu, and A. G. Yodh, Phys. Rev. Lett. **105**, 025501 (2010).
[30] D. Z. Rocklin, S. Zhou, K. Sun, and X. Mao, Nat. Commun. **8**, 14201 (2017).
[31] V. K. de Souza and P. Harrowell, Proc. Natl. Acad. Sci. U.S.A. **106**, 15136 (2009).
[32] J. W. Rocks, N. Pashine, I. Bischofberger, C. P. Goodrich, A. J. Liu, and S. R. Nagel, Proc. Natl. Acad. Sci. U.S.A. **114**, 2520 (2017).
[33] L. Yan, R. Ravasio, C. Brito, and M. Wyart, Proc. Natl. Acad. Sci. U.S.A. **114**, 2526 (2017).
[34] K. E. Dunn, F. Dannenberg, T. E. Ouldridge, M. Kwiatkowska, A. J. Turberfield, and J. Bath, Nature (London) **525**, 82 (2015).
[35] G. Nava, M. Rossi, S. Biffi, F. Sciortino, and T. Bellini, Phys. Rev. Lett. **119**, 078002 (2017).
[36] D. Z. Rocklin, V. Vitelli, and X. Mao, arXiv:1802.02704.
[37] X. Mao, A. Souslov, C. I. Mendoza, and T. C. Lubensky, Nat. Commun. **6**, 5968 (2015).
[38] L. Zhang and X. Mao, Phys. Rev. E **93**, 022110 (2016).
[39] H. Shen, P. Tan, and L. Xu, Phys. Rev. Lett. **116**, 048302 (2016).
[40] L. M. Nash, D. Kleckner, A. Read, V. Vitelli, A. M. Turner, and W. T. M. Irvine, Proc. Natl. Acad. Sci. U.S.A. **112**, 14495 (2015).
[41] P. Wang, L. Lu, and K. Bertoldi, Phys. Rev. Lett. **115**, 104302 (2015).
[42] A. Souslov, B. C. van Zuiden, D. Bartolo, and V. Vitelli, Nat. Phys. **13**, 1091 (2017).
[43] P. Ronceray, C. P. Broedersz, and M. Lenz, Proc. Natl. Acad. Sci. U.S.A. **113**, 2827 (2016).
[44] S. Stam, S. L. Freedman, S. Banerjee, K. L. Weirich, A. R. Dinner, and M. L. Gardel, Proc. Natl. Acad. Sci. U.S.A. **114**, E10037 (2017).
[45] D. L. Koch and G. Subramanian, Annu. Rev. Fluid Mech. **43**, 637 (2011).
[46] M. C. Marchetti, J.-F. Joanny, S. Ramaswamy, T. B. Liverpool, J. Prost, M. Rao, and R. A. Simha, Rev. Mod. Phys. **85**, 1143 (2013).
[47] C. Bechinger, R. Di Leonardo, H. Löwen, C. Reichhardt, G. Volpe, and G. Volpe, Rev. Mod. Phys. **88**, 045006 (2016).
[48] I. Rushkin, V. Kantsler, and R. E. Goldstein, Phys. Rev. Lett. **105**, 188101 (2010).
[49] C. Maggi, M. Paoluzzi, N. Pellicciotta, A. Lepore, L. Angelani, and R. Di Leonardo, Phys. Rev. Lett. **113**, 238303 (2014).
[50] É. Fodor, C. Nardini, M. E. Cates, J. Tailleur, P. Visco, and F. van Wijland, Phys. Rev. Lett. **117**, 038103 (2016).
[51] C. Battle, C. P. Broedersz, N. Fakhri, V. F. Geyer, J. Howard, C. F. Schmidt, and F. C. MacKintosh, Science **352**, 604 (2016).
[52] T. Franosch, M. Grimm, M. Belushkin, F. M. Mor, G. Foffi, L. Forró, and S. Jeney, Nature (London) **478**, 85 (2011).
[53] R. Di Leonardo, L. Angelani, D. DellArciprete, G. Ruocco, V. Iebba, S. Schippa, M. P. Conte, F. Mecarini, F. De Angelis, and E. Di Fabrizio, Proc. Natl. Acad. Sci. U.S.A. **107**, 9541 (2010).
[54] A. Sokolov, M. M. Apodaca, B. A. Grzybowski, and I. S. Aranson, Proc. Natl. Acad. Sci. U.S.A. **107**, 969 (2010).
[55] F. Schweitzer, W. Ebeling, and B. Tilch, Phys. Rev. Lett. **80**, 5044 (1998).
[56] U. Erdmann, W. Ebeling, L. Schimansky-Geier, and F. Schweitzer, Eur. Phys. J. B **15**, 105 (2000).
[57] A. Forrow, F. G. Woodhouse, and J. Dunkel, Phys. Rev. Lett. **119**, 028102 (2017).
[58] A. Bricard, J.-B. Caussin, N. Desreumaux, O. Dauchot, and D. Bartolo, Nature (London) **503**, 95 (2013).
[59] S. Krishnamurthy, S. Ghosh, D. Chatterji, R. Ganapathy, and A. K. Sood, Nat. Phys. **12**, 1134 (2016).
[60] A. A. Lee, D. Vella, and J. S. Wettlaufer, Proc. Natl. Acad. Sci. U.S.A. **114**, 9255 (2017).
[61] See Supplemental Material at http://link.aps.org/supplemental/10.1103/PhysRevLett.121.178001 for videos, methods, and detailed derivations, which includes Refs. [62–65].
[62] E. Jones, T. Oliphant, P. Peterson *et al.*, SciPy: Open Source Scientific Tools for Python, http://www.scipy.org/.
[63] C. J. Geyer, Stat. Sci. **7**, 473 (1992).
[64] T. J. Witt and N. E. Fletcher, Metrologia **47**, 616 (2010).
[65] D. B. Allan, T. Caswell, N. C. Keim, and C. M. van der Wel, Trackpy v0.4.1, https://doi.org/10.5281/zenodo.1226458.
[66] T. Sanchez, D. T. Chen, S. J. DeCamp, M. Heymann, and Z. Dogic, Nature (London) **491**, 431 (2012).
[67] C. Sandford and A. Y. Grosberg, Phys. Rev. E **97**, 012602 (2018).
[68] P. Jung and P. Hänggi, Phys. Rev. A **35**, 4464 (1987).
[69] C. Maggi, U. M. B. Marconi, N. Gnan, and R. Di Leonardo, Sci. Rep. **5**, 10742 (2015).
[70] S. Das, G. Gompper, and R. G. Winkler, New J. Phys. **20**, 015001 (2018).
[71] J. W. S. B. Rayleigh, *The Theory of Sound*, Vol. 2 (Macmillan, London, 1896).
[72] C. Sandford, A. Y. Grosberg, and J.-F. Joanny, Phys. Rev. E **96**, 052605 (2017).
[73] J. Toner and Y. Tu, Phys. Rev. E **58**, 4828 (1998).
[74] R. Fleury, D. L. Sounas, C. F. Sieck, M. R. Haberman, and A. Alù, Science **343**, 516 (2014).

Autonomous actuation of zero modes in mechanical networks far from equilibrium: Supplementary Material

Francis G. Woodhouse,[1,*] Henrik Ronellenfitsch,[2] and Jörn Dunkel[2]

[1] *Department of Applied Mathematics and Theoretical Physics, Centre for Mathematical Sciences, University of Cambridge, Wilberforce Road, Cambridge CB3 0WA, U.K.*

[2] *Department of Mathematics, Massachusetts Institute of Technology, 77 Massachusetts Avenue, Cambridge MA 02139-4307, U.S.A.*

SINGLE MASS

Low temperature expansion

Here, we evaluate the low temperature expansion of the energy

$$H(x,y) = \tfrac{1}{2}\left[(|(1-x,y)|-1)^2 + (|(1+x,y)|-1)^2\right]$$

corresponding to the simple bead-spring model in Fig. 1 of the main text.

To lowest order in x and y, the non-interacting terms in the expansion $H(x,y) = x^2 + \frac{1}{4}y^4 + \cdots$ imply scalings $x \sim T^{1/2}$, $y \sim T^{1/4}$. Let $x = T^{1/2}u$ and $y = T^{1/4}v$. Then, expanding H in powers of $T^{1/2}$, write

$$T^{-1}H(x,y) = h_0(u,v) + T^{1/2}h_1(u,v) + O(T),$$

where

$$h_0(u,v) = u^2 + \tfrac{1}{4}v^4, \qquad h_1(u,v) = -u^2v^2 - \tfrac{1}{8}v^6.$$

We seek an expansion in T for the moment

$$\langle x^m y^n\rangle = \frac{\int_{-\infty}^{\infty}\int_{-\infty}^{\infty} x^m y^n e^{-H/T}\,dx\,dy}{\int_{-\infty}^{\infty}\int_{-\infty}^{\infty} e^{-H/T}\,dx\,dy}.$$

First, consider the partition function Z in the denominator. Changing to u and v, this reads

$$Z = T^{3/4}\iint e^{-h_0(u,v)}e^{-T^{1/2}h_1(u,v)+O(T)}\,du\,dv. \quad \text{(S1)}$$

Define the integral

$$I[f(u,v)] = \iint f(u,v)e^{-h_0(u,v)}\,du\,dv.$$

Since $T \ll 1$, the leading exponent in Eq. (S1) decays much faster than any others. Thus Z can be approximated by expanding $e^{-T^{1/2}h_1+O(T)} = 1 - T^{1/2}h_1 + O(T)$ to obtain

$$Z = T^{3/4}\left\{I[1] - T^{1/2}I[h_1] + O(T)\right\}.$$

An identical derivation gives

$$\iint x^m y^n e^{-H/T}\,dx\,dy = T^{3/4+m/2+n/4}\left\{I[u^m v^n] - T^{1/2}I[u^m v^n h_1] + O(T)\right\}.$$

We can now assemble $\langle x^m y^n\rangle$. The above implies

$$T^{-m/2-n/4}\langle x^m y^n\rangle = \frac{I[u^m v^n] - T^{1/2}I[u^m v^n h_1] + O(T)}{I[1] - T^{1/2}I[h_1] + O(T)}.$$

Let $J[f] = I[f]/I[1]$. Expanding once more in T gives the general result

$$T^{-m/2-n/4}\langle x^m y^n\rangle = J[u^m v^n] - T^{1/2}\left\{J[u^m v^n h_1] - J[u^m v^n]J[h_1]\right\} + O(T).$$

Thus the expansion amounts to the moment in the bare non-interacting Hamiltonian $H_0 = x^2 + \frac{1}{4}y^4$ corrected by its covariance with the strongest interactions.

Particular cases may be computed by evaluating the integrals. This can be done symbolically for general m, n; the particular cases of $\langle x^2\rangle$ and $\langle y^2\rangle$ read

$$\langle x^2\rangle = \frac{1}{2}T + \rho T^{3/2} + O(T^2),$$
$$\langle y^2\rangle = 2\rho T^{1/2} + \left\{\frac{9}{8} - \frac{7\rho^2}{2}\right\}T + O(T^{3/2}),$$

with $\rho = \Gamma(3/4)/\Gamma(1/4) \approx 0.34$.

Correlated noise: small τ

Upon introducing exponentially correlated noise generated by independent Ornstein–Uhlenbeck processes, the statistical distribution of the bead changes. We specialise to the overdamped limit, and rescale time to set $\gamma = 1$. Through an expansion in the correlation time τ, Ref. [1] shows that the mass follows an effective potential

$$H_{\text{eff}} = H + \tau\left[\tfrac{1}{2}|\boldsymbol{\nabla}H|^2 - T\nabla^2 H\right] + O(\tau^2). \quad \text{(S2)}$$

For the single bead, the full potential $H(x,y)$ can be substituted and moments of H_{eff} numerically evaluated, as shown in Fig. 1 of the main text with moments evaluated by quadrature in Mathematica.

To see the essential behaviour, we use expansion techniques at low temperature and small τ. When $T \ll 1$, the scaling $x \sim T^{1/2}$, $y \sim T^{1/4}$ still holds provided τ is small. Given this, the leading order terms read

$$H_{\text{eff}} = (\text{const}) + (1+2\tau)x^2 + \frac{1}{4}y^4 + \cdots$$

Thus the base effect of τ is to tighten the stiffness in x but leave y unchanged. This leading-order behaviour can also be captured by the unified coloured noise approximation [2, 3].

Provided the additional T factor in H_{eff} is carefully accounted for, the same low-temperature expansion as in the thermal case above can be applied. Omitting the irrelevant constant, H_{eff} has expansion terms

$$h_0(u,v) = (1+2\tau)u^2 + \tfrac{1}{4}v^4,$$
$$h_1(u,v) = -(1+4\tau)u^2v^2 - (\tfrac{1}{8} - \tfrac{1}{2}\tau)v^6 - \tau v^2.$$

Note the emergent v^2 term at non-zero τ in h_1, which will act to confine fluctuations in y as the temperature increases. Performing the integrations and expanding in τ eventually gives the leading order dependence of the variance ratio as

$$\frac{\langle y^2\rangle}{\langle x^2\rangle} = 4\rho(1+2\tau)T^{-1/2} + \tfrac{9}{4} - 15\rho^2 - \left(50\rho^2 - \tfrac{7}{2}\right)\tau + O(T^{1/2}).$$

Recasting this as a series first in τ, namely

$$\frac{\langle y^2\rangle}{\langle x^2\rangle} = 4\rho T^{-1/2} + \tfrac{9}{4} - 15\rho^2 + \left(8\rho T^{-1/2} - 50\rho^2 + \tfrac{7}{2}\right)\tau + \cdots$$

reveals the temperature-dependent effect of correlation.

Correlated noise: large τ

In the limit of large τ, we can appeal to separation of equilibration time scales to derive an approximate distribution for the position $\boldsymbol{x} = (x, y)$.

In the overdamped limit, as before, $\boldsymbol{x}$ obeys

$$\dot{\boldsymbol{x}} = -\boldsymbol{\nabla}H(\boldsymbol{x}) + \boldsymbol{\xi}, \tag{S3}$$
$$\tau\dot{\boldsymbol{\xi}} = -\boldsymbol{\xi} + \boldsymbol{\eta}. \tag{S4}$$

First, Eq. (S4) implies that the stationary distribution of $\boldsymbol{\xi}$ is normal, with p.d.f. $p_{\boldsymbol{\xi}}(\boldsymbol{\xi}) \propto e^{-\tau|\boldsymbol{\xi}|^2/2T}$. Now, when τ is large, $\boldsymbol{x}$ equilibrates much faster than $\boldsymbol{\xi}$. Thus given the distribution of $\boldsymbol{\xi}$ we can approximate that of $\boldsymbol{x}$ by assuming $\dot{\boldsymbol{x}} \approx 0$ on time scales comparable with τ. Thus Eq. (S3) gives the relationship $\boldsymbol{\xi} \approx \boldsymbol{\nabla}H(\boldsymbol{x})$ between $\boldsymbol{\xi}$ and $\boldsymbol{x}$. Given $p_{\boldsymbol{\xi}}$, we can therefore approximate the p.d.f. $p_{\boldsymbol{x}}(\boldsymbol{x})$ of $\boldsymbol{x}$ through the inversion formula

$$p_{\boldsymbol{x}}(\boldsymbol{x}) = ||\boldsymbol{\nabla}\boldsymbol{\nabla}H||\, p_{\boldsymbol{\xi}}(\boldsymbol{\nabla}H(\boldsymbol{x})) \propto ||\boldsymbol{\nabla}\boldsymbol{\nabla}H||\, e^{-\tau|\boldsymbol{\nabla}H(\boldsymbol{x})|^2/2T}, \tag{S5}$$

where $||\boldsymbol{\nabla}\boldsymbol{\nabla}H||$ denotes the absolute value of the determinant of the Hessian $\boldsymbol{\nabla}\boldsymbol{\nabla}H$ (that is, the Jacobian of the transformation by $\boldsymbol{\nabla}H$).

For $\tau/T \gg 1$ we can, like before, take an expansion to approximate moments of this distribution. Provided one accounts for the prefactor of the exponential, moments of $p_{\boldsymbol{x}}$ are related to moments of the Boltzmann distribution with effective potential $G(\boldsymbol{x}) = \frac{1}{2}|\boldsymbol{\nabla}H(\boldsymbol{x})|^2$ and effective temperature $T' = T/\tau$, since $p_{\boldsymbol{x}} \propto ||\boldsymbol{\nabla}\boldsymbol{\nabla}H||e^{-G/T'}$. Now, G has leading non-interacting terms $G = 2x^2 + \frac{1}{2}y^6 + \cdots$ implying scalings $x \sim T'^{1/2}$ and $y \sim T'^{1/6}$ (cf. the small-τ scalings $x \sim T^{1/2}$ and $y \sim T^{1/4}$). Following the same process as the low temperature expansion, by substituting for $x = T'^{1/2}u$ and $y = T'^{1/6}v$ and expanding in powers of $T'^{1/3}$ moments can be approximated as an expansion in T'. For conciseness we just compute the leading order here. We have

$$||\boldsymbol{\nabla}\boldsymbol{\nabla}H||e^{-G/T'} = \left[6v^2T'^{1/3} + O(\beta^{-2/3})\right]e^{-2u^2-v^6/2},$$

implying

$$\iint x^m y^n p_{\boldsymbol{x}}(\boldsymbol{x})\,dx\,dy \approx 6T'^{2/3+m/2+n/6}\iint u^m v^{2+n} e^{-2u^2-v^6/2}\,du\,dv.$$

Thus the normalisation Z for the p.d.f. $||\boldsymbol{\nabla}\boldsymbol{\nabla}H||e^{-G/T'}$ is

$$Z \approx 6T'^{2/3}\iint v^2 e^{-2u^2-v^6/2}\,du\,dv = 2\pi T'^{2/3}$$

and the variances are

$$\langle x^2\rangle \approx \frac{6T'^{5/3}}{Z}\iint u^2v^2e^{-2u^2-v^6/2}\,du\,dv = \frac{T'}{4},$$
$$\langle y^2\rangle \approx \frac{6T'}{Z}\iint v^4e^{-2u^2-v^6/2}\,du\,dv = \frac{2^{1/3}\Gamma(5/6)}{\pi^{1/2}}T'^{1/3}.$$

To lowest order, the variance ratio $\langle y^2\rangle/\langle x^2\rangle$ for large τ/T is therefore

$$\frac{\langle y^2\rangle}{\langle x^2\rangle} \approx \frac{2^{7/3}\Gamma(5/6)}{\pi^{1/2}}\left(\frac{\tau}{T}\right)^{2/3}.$$

As well as giving the power law for large τ, this shows that the T-dependence of the variance ratio changes from $T^{-1/2}$ at small τ to $T^{-2/3}$ at large τ. This is driven by the change in form of G compared to H: the prefactor $||\boldsymbol{\nabla}\boldsymbol{\nabla}H||$ does not affect the dominant scaling of the moments, so they scale with T as they would in the potential G.

NETWORKS: NON-DIMENSIONALISATION

The full dimensional equations of motion read

$$m\ddot{\boldsymbol{x}}_\alpha = -\frac{\partial H}{\partial \boldsymbol{x}_\alpha} - \gamma\dot{\boldsymbol{x}}_\alpha + \boldsymbol{F}_\alpha(\dot{\boldsymbol{x}}_\alpha; t),$$

with energy

$$H(\{\boldsymbol{x}_\alpha\}) = \frac{1}{2}\sum_{(\alpha,\beta)} k_{\alpha\beta}(|\boldsymbol{x}_\alpha - \boldsymbol{x}_\beta| - \ell_{\alpha\beta})^2.$$

Let κ and λ be typical scales for the spring moduli $k_{\alpha\beta}$ and rest lengths $\ell_{\alpha\beta}$. Rescale space and time as $\boldsymbol{x}_\alpha = \lambda\tilde{\boldsymbol{x}}_\alpha$ and $t = \tilde{t}\sqrt{m/\kappa}$, and use primes to denote $d/d\tilde{t}$. Then

$$\tilde{\boldsymbol{x}}''_\alpha = -\frac{\partial\tilde{H}}{\partial\tilde{\boldsymbol{x}}_\alpha} - \tilde{\gamma}\tilde{\boldsymbol{x}}'_\alpha + \tilde{\boldsymbol{F}}_\alpha(\tilde{\boldsymbol{x}}'_\alpha;\tilde{t}),$$

with dimensionless energy

$$\tilde{H}(\{\tilde{\boldsymbol{x}}_\alpha\}) = \frac{1}{2}\sum_{(\alpha,\beta)} \tilde{k}_{\alpha\beta}(|\tilde{\boldsymbol{x}}_\alpha - \tilde{\boldsymbol{x}}_\beta| - \tilde{\ell}_{\alpha\beta})^2$$

and dimensionless parameters

$$\tilde{\gamma} = \gamma/\sqrt{m\kappa}, \quad \tilde{k}_{\alpha\beta} = k_{\alpha\beta}/\kappa, \quad \tilde{\ell}_{\alpha\beta} = \ell_{\alpha\beta}/\lambda.$$

Note that the particle mass m has been scaled to unity. The dimensionless forcing function $\tilde{\boldsymbol{F}}_\alpha$ relates to the dimensional forcing through $\tilde{\boldsymbol{F}}_\alpha = (\kappa\lambda)^{-1}\boldsymbol{F}_\alpha(\lambda\sqrt{\kappa/m}\tilde{\boldsymbol{x}}'_\alpha; t\sqrt{m/\kappa})$.

Rescaling of noise

For white noise, $\boldsymbol{F}_\alpha = \boldsymbol{\eta}_\alpha(t)$ with $\langle\eta_{\alpha i}(t)\eta_{\beta j}(t')\rangle = 2\gamma T\delta_{\alpha\beta}\delta_{ij}\delta(t-t')$. Under our rescaling, this becomes another white noise $\tilde{\boldsymbol{F}}_\alpha = \tilde{\boldsymbol{\eta}}_\alpha(\tilde{t})$ correlated as $\langle\eta_{\alpha i}(t)\eta_{\beta j}(t')\rangle = 2\tilde{\gamma}\tilde{T}\delta_{\alpha\beta}\delta_{ij}\delta(t-t')$, with dimensionless temperature $\tilde{T} = T/(\kappa\lambda^2)$.

For exponentially correlated noise, $\boldsymbol{F}_\alpha = \boldsymbol{\xi}_\alpha(t)$ with $\langle\xi_{\alpha i}(t)\xi_{\beta j}(t')\rangle = \gamma T\delta_{\alpha\beta}\delta_{ij}e^{-|t-t'|/\tau}/\tau$. Under our rescaling, this becomes a process $\tilde{\boldsymbol{F}}_\alpha = \tilde{\boldsymbol{\xi}}_\alpha(\tilde{t})$ correlated as $\langle\tilde{\xi}_{\alpha i}(\tilde{t})\tilde{\xi}_{\beta j}(\tilde{t}')\rangle = \tilde{\gamma}\tilde{T}\delta_{\alpha\beta}\delta_{ij}e^{-|\tilde{t}-\tilde{t}'|/\tilde{\tau}}/\tilde{\tau}$ with dimensionless temperature $\tilde{T} = T/(\kappa\lambda^2)$ and correlation time $\tilde{\tau} = \tau\sqrt{\kappa/m}$. This becomes the white noise process above in the limit $\tilde{\tau}\to 0$.

Active forcing $\boldsymbol{F}_\alpha = \gamma_f\dot{\boldsymbol{x}}_\alpha(1 - |\dot{\boldsymbol{x}}_\alpha|^2/v^2)$ rescales to $\tilde{\boldsymbol{F}}_\alpha = \tilde{\gamma}_f\tilde{\boldsymbol{x}}'_\alpha(1 - |\tilde{\boldsymbol{x}}'_\alpha|^2/\tilde{v}^2)$ with dimensionless active friction coefficient $\tilde{\gamma}_f = \gamma_f/\sqrt{\kappa m}$ and target speed $\tilde{v} = \lambda\sqrt{\kappa/m}v$.

NETWORKS: HM–ZM COUPLING

Low temperature expansion

The symmetry of the single-mass example means that the HM and ZM decouple in the limit $T\to 0$. However, this is not necessarily the case in general: in a potential where x^2 and y^4 both scale with T, interaction terms xy^2 will also scale with T. Consider now a system of $n+1$ degrees of freedom $\{x_1,\ldots,x_n,y\}$, where the n variables x_i are HMs and y is a quartic IZM. In a low temperature expansion, the potential energy is

$$H = \sum_i a_i x_i^2 + \sum_i b_i x_i y^2 + Ay^4 \tag{S6}$$

at lowest order, where $A>0$ and all $a_i>0$ but each b_i can be of either sign. We will evaluate the amplitudes $\langle y^2\rangle$ and $\langle x_i^2\rangle$.

To compute $\langle y^2\rangle$, we can split the Boltzmann factor $e^{-H/T}$ into factors which can be integrated in each coordinate x_i sequentially, writing

$$e^{-H/T} = e^{-Ay^4/T}\prod_i e^{-(a_i x_i^2 + b_i x_i y^2)/T}.$$

Since

$$\int dx_i\, e^{-(a_i x_i^2 + b_i x_i y^2)/T} = C_i e^{(b_i^2/4a_i)y^4/T}$$

with $C_i = \sqrt{\pi T/a_i}$, splitting the Boltzmann factor allows us to reduce the computation to

$$\langle y^2\rangle = \frac{\int dy\, y^2 e^{-Ay^4/T}\prod_i C_i e^{(b_i^2/4a_i)y^4/T}}{\int dy\, e^{Ay^4/T}\prod_i C_i e^{(b_i^2/4a_i)y^4/T}}.$$

The constant factors cancel and the exponentials combine, giving

$$\langle y^2\rangle = \frac{\int dy\, y^2 e^{-\tilde{A}y^4/T}}{\int dy\, e^{-\tilde{A}y^4/T}} = \rho\sqrt{T/\tilde{A}},$$

where

$$\tilde{A} = A - \sum_i \frac{b_i^2}{4a_i}$$

and $\rho = \Gamma(3/4)/\Gamma(1/4)$ as before. That is, the variance $\langle y^2\rangle$ is simply that of a single degree of freedom in an effective quartic potential $\tilde{A}y^4$. Note that $\tilde{A} < A$: the HM coupling increases the ZM amplitude.

The computation for $\langle x_m^2\rangle$ is similar, albeit not quite as clean since the integral in x_m must incorporate the x_m^2 factor. Using the integral

$$\int dx_m x_m^2 e^{-(a_m x_m^2 + b_m x_m y^2)/T} = C_m e^{(b_m^2/4a_m)y^4/T}\left(\frac{b_m^2}{4a_m^2}y^4 + \frac{T}{2a_m}\right),$$

the same approach as for $\langle y^2\rangle$ reduces the computation to

$$\langle x_m^2\rangle = \frac{\int dy\, \left(\frac{b_m^2}{4a_m^2}y^4 + \frac{T}{2a_m}\right)e^{-\tilde{A}y^4/T}}{\int dy\, e^{-\tilde{A}y^4/T}},$$

which is again simply a combination of moments in the effective potential $\tilde{A}y^4$. Thus

$$\langle x_m^2 \rangle = \frac{T}{2a_m}\left(1 + \frac{b_m^2}{8\tilde{A}a_m}\right). \tag{S7}$$

Observe that $\langle x_m^2 \rangle$ is only ever increased by introducing interactions b_m compared to its uncoupled amplitude $T/2a_m$. Thus not only do HM–ZM couplings increase ZM fluctuations, but they concomitantly increase HM fluctuations above those that would be guessed from naive equipartition. This effect is illustrated in Fig. S1 for 20 HMs of the network in Fig. 2 of the main text, for which interaction coefficients were determined by series expansion of the elastic energy in Mathematica.

There is one further effect to be noted. Not only does coupling increase the second moment $\langle x_m^2 \rangle$, but the mean $\langle x_m \rangle$ is displaced from zero by the asymmetry of the coupling. The same techniques again can be used to compute $\langle x_m \rangle$, this time using the integral

$$\int dx_m x_m e^{-(a_m x_m^2 + b_m x_m y^2)/T} = -C_m e^{(b_m^2/4a_m)y^4/T} \frac{b_m}{2a_m} y^2,$$

giving

$$\langle x_m \rangle = \frac{b_m}{2a_m}\langle y^2 \rangle = \frac{b_m}{2a_m}\rho\sqrt{T/\tilde{A}}.$$

Conversely, the ZM is not displaced: symmetry means $\langle y \rangle = 0$.

The interaction-driven increase in $\langle x_m^2 \rangle$ could potentially be just a side effect of the non-zero mean $\langle x_m \rangle$. However, combining these results gives the mode variance as

$$\mathrm{Var}(x_m) = \frac{T}{2a_m}\left(1 + \frac{(1-4\rho^2)b_m^2}{8\tilde{A}a_m}\right).$$

Since $1 - 4\rho^2 \approx 0.54 > 0$, the variance is indeed increased by HM–ZM coupling despite the shifted mean.

Correlated noise: small τ

When weak correlated noise is introduced into a general system with multiple HMs coupled to a ZM, its effect on the ZM can be neglected at low temperatures and short correlation times. The calculation goes as follows.

Take the same energy form as in Eq. (S6). Following Ref. [1] as in the single-mass example, when weak correlated noise of non-zero correlation time $\tau \ll 1$ is introduced the system follows an effective energy given by Eq. (S2). At low temperature, where $x^2 \sim T$ and $y^4 \sim T$, evaluating the gradients and keeping only the lowest order terms gives a first-order adjusted energy

$$H_{\text{eff}} = \sum_i a_i' x_i^2 + \sum_i b_i' x_i y^2 + A' y^4$$

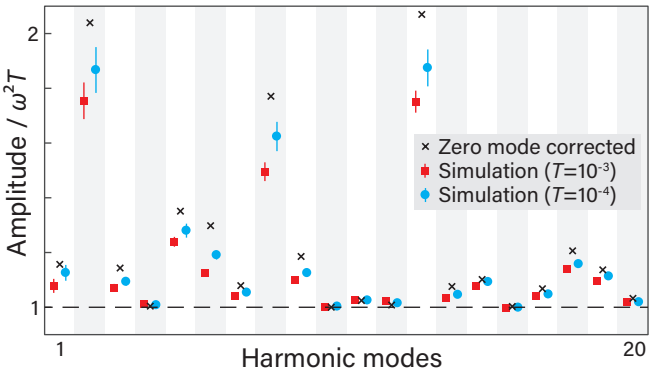

FIG. S1. Deviation from naive equipartition of the first 20 lowest-frequency HMs of the network in Fig. 2 of the main text. Markers show normalised amplitude $\langle c_i^2 \rangle / \omega_i^2 T$ numerically evaluated at $T = 10^{-3}$ (red squares) and $T = 10^{-4}$ (blue circles) compared to naive equipartition at 1 (dashed line) and with first-order correction in Eq. (S7) for interactions with the ZM (black cross). Error bars are estimated 95% confidence intervals. Interaction coefficients were determined by series expansion of the elastic energy in Mathematica.

where the τ-adjusted coefficients read

$$a_i' = a_i(1 + 2\tau a_i),$$
$$A' = A + \tfrac{1}{2}\tau \sum_i b_i^2,$$
$$b_i' = b_i(1 + 2\tau a_i).$$

It is clear that correlation $\tau > 0$ strengthens all couplings: $a_i' > a_i$, $A' > A$ and $|b_i'| > |b_i|$.

The approximate ZM amplitude $\langle y^2 \rangle$ is given by substituting these adjusted couplings into the formulae computed above. But, on computing the coupling-adjusted ZM amplitude

$$\tilde{A}' = A' - \sum_i \frac{{b_i'}^2}{4a_i'},$$

it transpires that $\tilde{A}' = \tilde{A}$. Since only this and T determine $\langle y^2 \rangle$, to first order in τ, the effect of correlations on the HMs is precisely compensated by its effect on the coupling terms to leave the ZM amplitude unchanged, that is, $\langle y^2 \rangle = \langle y^2 \rangle_{\tau=0}$ for $\tau \ll 1$.

Correlated noise: large τ

At large τ, the same timescale separation arguments as for the single bead can be used to derive asymptotic scalings for mode amplitudes in the overdamped limit. We sketch here the basic argument.

Once again take the same energy form as in Eq. (S6), this time appealing to a low $T' = T/\tau$ expansion. When τ is large, the mode degrees of freedom x_i and y equilibrate with the coloured noise much faster than the noise

changes. Equation (S5) then gives the effective p.d.f. for the modes. In this distribution, the scaling of the modes is driven by the exponential factor $e^{-G/T'}$ with potential $G(x_1,\ldots,x_n,y)=\frac{1}{2}|\boldsymbol{\nabla}H|^2$, where

$$G=\sum_i \tfrac{1}{2}\left(2a_ix_i+b_iy^2\right)^2+\tfrac{1}{2}y^2\left(\sum_i 2b_ix_i+4Ay^2\right)^2.$$

From a naive look at G one might infer that $x_i\sim T'^{1/2}$ and $y\sim T'^{1/4}$ (provided at least one $b_i\neq 0$) because of the non-interacting x_i^2 and y^4 terms at lowest order. However, there is an important subtlety: because the terms in the first sum, which are the lowest order terms, can be factorised as written, changing variables from x_i to $z_i=2a_ix_i+b_iy^2$ eliminates y from the sum while only contributing a constant Jacobian factor to moment integrals. In other words, scalings are governed by the transformed potential

$$\tilde{G}=\sum_i \tfrac{1}{2}z_i^2+\tfrac{1}{2}y^2\left(\sum_i \frac{b_i}{a_i}(z_i-b_iy^2)+4Ay^2\right)^2.$$

Under $\tilde{G}$, the lowest non-interacting terms are z_i^2 and y^6. Thus $y\sim T'^{1/6}$—not $T'^{1/4}$—and $z_i\sim T'^{1/2}$, together implying $x_i\sim T'^{1/2}$. Therefore, the amplitudes $\langle x_i^2\rangle$ and $\langle y^2\rangle$ are asymptotically proportional to (T/τ) and $(T/\tau)^{1/3}$, respectively.

This argument shows that interaction terms do not affect the asymptotic scaling of the ZM and HMs with T/τ, with the ZM dominating HMs by a factor $\langle y^2\rangle/\langle x_i^2\rangle\sim\tau^{2/3}$ for large τ. Exact moments $\langle x_i^2\rangle$ and $\langle y^2\rangle$ can be formulated by the same process of telescoping x_i-integrals as above, but it is significantly more algebraically unwieldy due to the more complex exponent and the prefactor of

$$||\boldsymbol{\nabla}\boldsymbol{\nabla}H||\propto\sum_i 2b_ix_i+\left(12A-\prod_j\frac{2b_j^2}{a_j}\right)y^2$$

in Eq. (S5). We therefore do not compute the exact moment formulae here.

NETWORKS: FURTHER EXAMPLES

In Fig. 2 of the main text, a network with a single IZM is used to exemplify actuation by active correlated noise. In Fig. S2 we extend this to large correlation $\tau=200$ and add two further examples displaying the same τ-dependent mode amplitude behaviour of HM suppresion and ZM preservation. At long correlation times the amplitude asymptotics derived above for HMs ($\langle x_i^2\rangle\sim\tau^{-1}$) and the ZM ($\langle y^2\rangle\sim\tau^{-1/3}$) gradually take hold. Some modes are well into the long-τ regime by $\tau=200$ while others are slower to approach it due to stronger higher-order terms.

Conversely, Fig. S3 shows that under-coordinated nodes can induce bistability in the structure, adversely affecting the mode statistics. In particular, a 2-coordinated node participating in the shown IZM has two equal-energy locations, meaning that bistable state transitions are easily triggered by the ZM actuation. This can adversely affect mode statistics if not eliminated at design time. In this case, though, the second stable location of the node overlaps with another, meaning that incorporating repulsive interactions between masses would lessen or eliminate the problem.

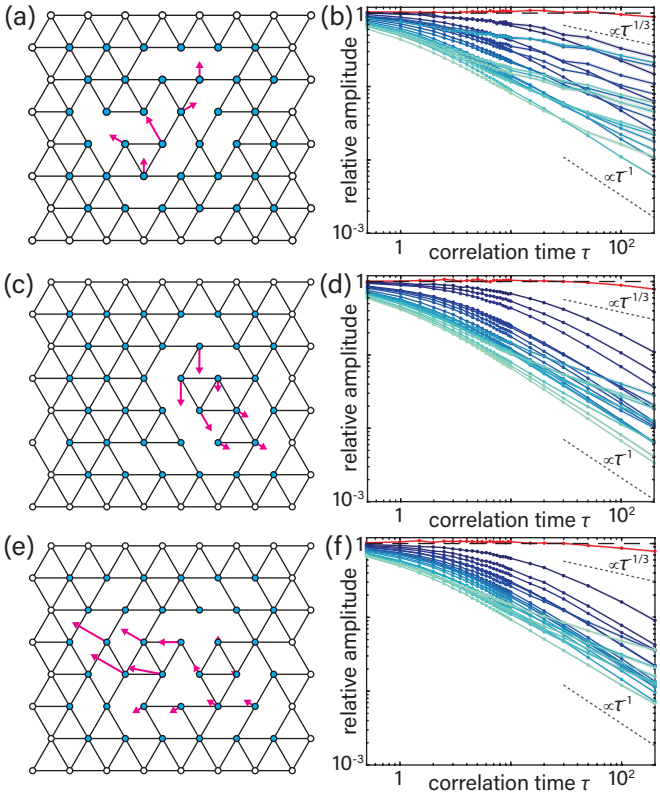

FIG. S2. Three examples of IZM actuation by correlated noise between $\tau=0.5$ and $\tau=200$. (a,c,e) Networks each with a single IZM (magenta) and pinned boundaries, with (a) as in Fig. 2 of the main text. (b,d,f) Thermal-relative mode amplitudes $\langle u_i^2\rangle_\tau/\langle u_i^2\rangle_{\tau=0}$ for the 21 lowest-eigenvalue modes of the networks in (a,c,e), on a log–log scale, with ZMs the uppermost red lines. Grey regions are approximate 95% confidence intervals; data computed from 20 independent realisations up to $t=2\times10^4$ with $\delta t=10^{-4}$ at values of τ between 0.5 and 200 indicated by points (see Computational Methods). Data in (a) is a superset of that of the main text Fig. 2(c), focussing here on large-τ behaviour. Shown gradient lines (dashed grey) are large-τ asymptotic predictions for the ZM ($\propto\tau^{1/3}$) and HMs ($\propto\tau$).

SELF-PROPULSIVE RAYLEIGH ACTIVITY

A mechanical network with Rayleigh activity has equations of motion

$$\ddot{\boldsymbol{x}}_\alpha = -\boldsymbol{\nabla}_\alpha H - \gamma\dot{\boldsymbol{x}}_\alpha + \gamma_f(1 - |\dot{\boldsymbol{x}}_\alpha|^2/v^2)\dot{\boldsymbol{x}}_\alpha. \tag{S8}$$

The friction and active forcing can be condensed into a friction-like term as

$$\ddot{\boldsymbol{x}}_\alpha = -\boldsymbol{\nabla}_\alpha H - f(|\dot{\boldsymbol{x}}_\alpha|)\dot{\boldsymbol{x}}_\alpha,$$

where $f(u) = \gamma - \gamma_f + \gamma_f u^2/v^2$ is the effective friction coefficient. If $f(0) = \gamma - \gamma_f \equiv \gamma_0 < 0$, stationary states have negative effective friction and are unstable, with friction switching from negative to positive when $f(u) = 0$ at $|u| = v_0 \equiv \sqrt{|\gamma_0|/\gamma_f}v$. We can rewrite f in terms of γ_0 and v_0 as $f(u) = \gamma_0(1 - u^2/v_0^2)$.

Activation

As in the main text, considering a small perturbation of the rest state and decomposing into eigenmodes of the dynamical matrix gives linearised equations of motion in terms of the small mode amplitudes c_k with $|c_k| \ll 1$. For linearised Rayleigh friction, this gives

$$\ddot{c}_k = -\omega_k^2 c_k - \gamma_0\dot{c}_k.$$

Elementary analysis then shows that, provided $\gamma_0 < 0$, solutions $e^{\sigma t}$ have either a real 'overdamped' maximal growth rate $\max\sigma_k = \frac{1}{2}(|\gamma_0| + \sqrt{\gamma_0^2 - 4\omega_k^2})$ if $|\gamma_0| \geq 2\omega_k$, or a complex 'underdamped' growth rate with real part $\mathrm{Re}\,\sigma_k = |\gamma_0|/2$ if $|\gamma_0| < 2\omega_k$. Thus in either case, $\mathrm{Re}\,\sigma_k \geq |\gamma_0|/2$. The largest possible growth rate $\sigma_k = |\gamma_0|$ is achieved for a ZM, where $\omega_k = 0$.

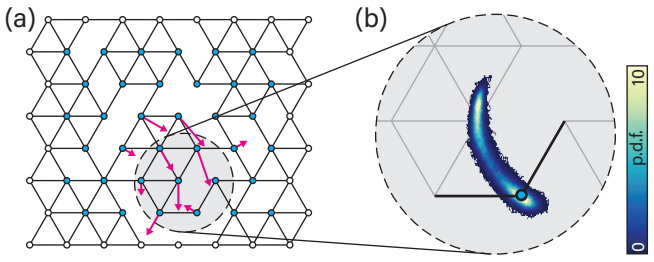

FIG. S3. Bistability in an IZM–participating node adds complexity to activation spectra. (a) A network with a single IZM, as before, containing a two-coordinated node whose position includes another equal-energy minimum by geometric symmetry. (b) Position histogram for the bistable node with $\tau = 6$. The node fluctuates into its other minimum, near which the overall mode spectrum is different. Note that in this case the bistability could be lessened by including hard-core repulsions between nodes.

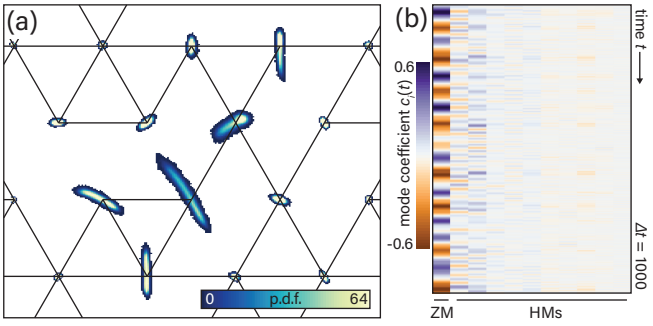

FIG. S4. Self-propulsive activity actuates IZMs in an oscillatory fashion (SM Video 4). (a) Per-node position histogram for the same network region as in Fig. 2b of the main text, but now actuated through Rayleigh forcing as in Eq. (S8). The ZM is prominent, while other nodes barely fluctuate. Parameters are $v_0 = 0.02$, $\gamma_0 = 1$, and $k_{\alpha\beta} = 1$, integrated at $\delta t = 10^{-5}$. (b) Example time trace over $\Delta t = 1000$ for the instance shown in (a) of mode coefficients $c_i(t)$ for the ZM and the ten lowest-frequency HMs. The ZM shows far stronger maxima than the HMs, with notable oscillatory behaviour.

Single mass: small γ_0

Unless mode k is a mechanism, growth of the mode will eventually be arrested by the combination of elastic forces and nonlinear effective friction terms, giving finite-amplitude oscillations. For the bead–spring example in the main text, we briefly examine this arrest process for small γ_0.

Formally, approximate solution for small $\epsilon \equiv |\gamma_0|$ is achieved by series expansion $\boldsymbol{x}(t) = \boldsymbol{x}_0(t) + \epsilon\boldsymbol{x}_1(t) + \cdots$. At $O(1)$, the equations of motion imply

$$\ddot{\boldsymbol{x}}_0 = -\boldsymbol{\nabla}H(\boldsymbol{x}_0).$$

Thus $\boldsymbol{x}_0$ simply corresponds to motion in the potential H, meaning $E_0 \equiv \frac{1}{2}|\dot{\boldsymbol{x}}_0|^2 + H(\boldsymbol{x}_0)$ is conserved.

Now, the range of maximum spatial extent occurs where $\dot{\boldsymbol{x}}_0 \sim 0$. Furthermore, higher-order dynamics set the velocity scale as $|\dot{\boldsymbol{x}}_0| \sim v_0$. Therefore, assuming $H(0) = 0$ is the energy minimum, conservation of E_0 between the origin and maximum extent implies $v_0^2 \sim H(\boldsymbol{x}_0)$ at the boundary. If v_0 is small, H can be approximated by its leading order expansion $H(x, y) \approx x^2 + \frac{1}{4}y^4$, meaning $y \sim v_0^{1/2}$ and $x \sim v_0$. Thus the variance ratio $\langle y^2\rangle/\langle x^2\rangle \sim 1/v_0$, and so the zero mode dominates as $v_0 \to 0$, fulfilling the same role as $T \to 0$ in the noise-driven case. (Indeed even with the same effective $1/\sqrt{T}$ scaling, since v_0^2 is a kinetic energy scale and so corresponds to T.)

Network IZM actuation

The same simultaneous ZM actuation and HM suppression in networks driven by active correlated noise

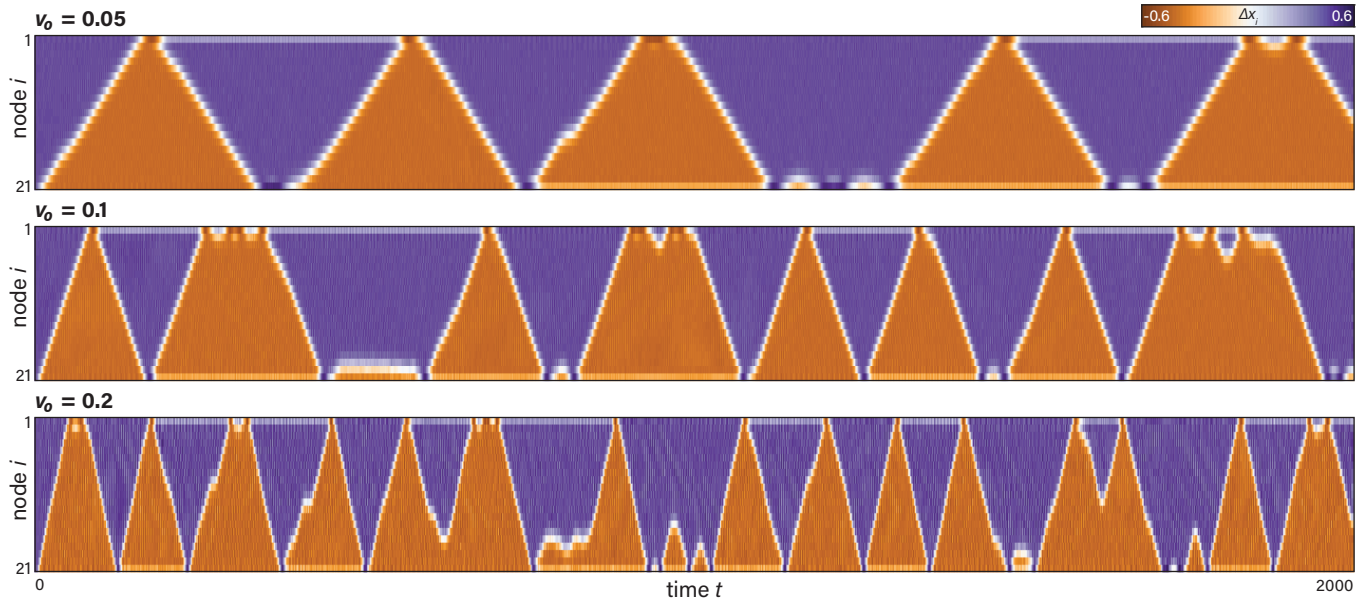

FIG. S5. Active mechanical SSH model as in Fig. 4 of the main text, with a different random perturbation to the initial conditions and 4× longer time window.

persists with Rayleigh self-propulsive activity, as illustrated in Fig. S4a (see also SM Video 4). The mode coefficients $c_i(t)$ have oscillatory temporal structure (Fig. S4b), giving potentially useful actuation behaviour that can be controlled by varying parameters of the activity.

Active mechanical SSH soliton

In Fig. 4 of the main text, we show realisations of the mechanical SSH model with self-propulsive activity at three different effective propulsion speeds v_0, exemplifying how activity excites the underlying mechanism leading to a self-propelled soliton-like domain boundary. While the domain propagates cleanly most of the time, there are occasional defects visible where the domain slows, stalls or reverses because of the complex interactions between the activity-driven oscillatory fluctuations of the nodes (main text Fig. 4b, $v_0 = 0.1$ and $v_0 = 0.2$). These imperfection phenomena can be seen in more detail in Fig. S5, where we exhibit a longer-time run of the same model and parameters as in the main text with a different random perturbation to the initial conditions. Stalls and reversals mid-chain are rare, with the endpoints being, perhaps unsurprisingly, more prone to imperfection because of the particular complexity of the mechanism there. We emphasise that this model does not have any random noise added, beyond an initial perturbation; these reversals are the result of complex interactions between the fluctuating self-propelled nodes.

COMPUTATIONAL METHODS

Single bead statistics

High-quality independent position samples for the single mass in Fig. 1 of the main text were computed by integrating the coupled overdamped equations

$$\dot{\boldsymbol{x}} = -\boldsymbol{\nabla} H(\boldsymbol{x}) + \boldsymbol{\xi}, \quad \tau\dot{\boldsymbol{\xi}} = -\boldsymbol{\xi} + \boldsymbol{\eta},$$

with $\langle \eta_i(t)\eta_j(t')\rangle = 2T\delta_{ij}\delta(t-t')$, up to a stopping time $t = t_{\mathrm{stop}}$ and taking the endpoint $\boldsymbol{x}(t = t_{\mathrm{stop}})$ as a sample. Taking a large set of N samples was accelerated by massively parallel GPU computing to perform each integration in one GPU thread (NVIDIA Titan X Pascal).

Network design

We design networks containing isolated IZMs by direct numerical minimisation of the lowest eigenvalue ω_1^2 of the dynamical matrix D_{ij} with respect to the stiffnesses $k_{\alpha\beta}$. Starting from uniformly random initial stiffnesses on a triangular lattice and constraining them to $0 \le k_{\alpha\beta} \le 1$, the gradient-based L-BFGS-B algorithm as implemented in SciPy 1.0 [4] generally converges to a network in which some of the stiffnesses and ω_1^2 are exactly zero, and which therefore exhibits an IZM. Since IZMs are topological, independent of the precise values of the nonzero $k_{\alpha\beta}$ [5], a network containing the same IZM is then obtained by removing the zero-stiffness bonds and setting the remaining stiffnesses to 1.

Network simulations

All numerical integration for networks was performed by Euler/Euler–Maruyama integration of the appropriate system of equations. Mode statistics were determined from M independent trajectories. Each trajectory was started from equilibrium, integrated over a time 100 and discarded to randomise initial conditions, and then sampled up to a time $t = t_{\max}$. The parameters M and $t_{\max}$ are given in figure captions.

Each trajectory was subsampled at a resolution $\Delta t = 1$ to compute statistics on $n = t_{\max}$ samples. The variance $\bar{\sigma}_i^2$ of the mean $\bar{x}$ of a statistic x computed from trajectory i was estimated through [6, 7],

$$\bar{\sigma}_i^2 = \frac{\sigma_i^2}{\sqrt{n}}\left[1 - \frac{2}{n}\sum_{k=1}^{\lfloor\sqrt{n}\rfloor}(n-k)\rho_i(k)\right],$$

where $\rho_i(k)$ is the normalised naively-estimated autocorrelation at lag k and the upper truncation at $\lfloor\sqrt{n}\rfloor$ omits heavily biased autocorrelation estimates that are in practice expected to be near zero [6]. Per-trajectory errors are then combined as independent variances to yield the overall estimated standard error $\bar{\sigma}$ of $\bar{x}$. Approximate 95% intervals are shown in figures as $\bar{x} \pm 1.96\bar{\sigma}$.

EXPERIMENTAL METHODS

The stiff-jointed network in Fig. 3a of the main text was constructed using flat brackets of dimensions 3.66 cm × 0.75 cm which were laser cut from transparent acrylic of thickness 1.2 mm. For the pin joints connecting the brackets, 2–56 thread size, 1/2 in long nylon screws and nuts were used. Where only three or four brackets were jointed together, the joints were strengthened using nylon washers. The pins corresponding to the outermost nodes were fastened directly to a 9 in diameter circular plate, laser cut from acrylic of circa 1 cm thickness. The plate was then mounted on top of an Eminence Speakers Delta-12LFA, 12 in, 500 W speaker (Eminence Speaker LLC, Eminence KY), which was mounted on an optical table and driven using a Pyle PQA4100 amplifier (Pyle Audio, Brooklyn NY). Video was acquired at 1920 × 1080 pixels resolution and a frame rate of 30 Hz using an Olympus consumer digital camera (Olympus America Inc., Center Valley PA) at 40 mm focal length mounted on a tripod. The positions of the nodes were tracked using the `trackpy 0.4.1` package [8].

To actuate the network, the speaker was driven by a signal comprising a carrier frequency and Ornstein–Uhlenbeck noise with subsecond correlation. In these experiments, it is the carrier frequency actuation that is mimicking the active driving, not the added correlated noise, as interactions between the network and the shaken baseboard drive stochastic forcing. The correlated noise here functions instead as a crucial component to prevent sticking of the network in resonance-related metastable states, discussed below.

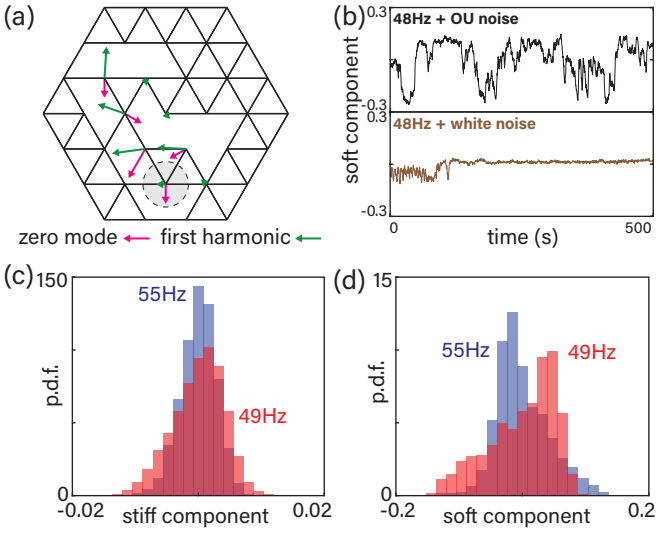

FIG. S6. Experimental actuation method affects relative ZM–HM statistics. (a) Diagram of the experimental network shown in the main text Fig. 3, with both the ZM and the lowest-frequency HM shown. (b) Traces of the soft component c_2, defined in the text, of the node highlighted in (a) for correlated and uncorrelated additions to 48 Hz carrier frequency actuation. The upper adds 15% Ornstein–Uhlenbeck noise of correlation time (1/350) s while the lower adds 15% white noise of identical intensity. Short-time correlation is necessary to keep the network exploring the energy landscape. (c,d) Histograms of soft (c) and stiff (d) components c_1 and c_2 for two frequenies of actuation, both with 20% added Ornstein–Uhlenbeck noise of correlation time (1/345) s. Changing the carrier frequency controls the mode actuation, with 55 Hz giving greater ZM actuation relative to non-ZM modes compared to 49 Hz. Note the 10× larger scale in the soft component (d) compared to the stiff component (c).

To explore the effect of different forms of drive, we focus on one particular node which participates in both the IZM and the lowest-frequency HM (highlighted in Fig. S6a) in near-perpendicular directions. Given its positions $\boldsymbol{x}_i = (x_i, y_i)$ at frames i, rescaled such that the distance between adjacent nodes is 1 in the reference configuration, we compute the covariance matrix $\mathrm{Cov}(x_i, y_i)$. The orthonormal eigenvectors $\boldsymbol{v}_1, \boldsymbol{v}_2$ of the covariance matrix corresponding to the eigenvalues $\lambda_1 < \lambda_2$ then represent the stiff ($\boldsymbol{v}_1$) and soft ($\boldsymbol{v}_2$) perpendicular directions. We then use the stiff and soft components $c_1 = \boldsymbol{x} \cdot \boldsymbol{v}_1$ and $c_2 = \boldsymbol{x} \cdot \boldsymbol{v}_2$ as simple representations of HM-related and ZM-dominated actuation.

Figure S6b shows the importance of short but non-zero correlation in the noise added to the carrier frequency. We compare the soft component c_2 from experiments using 48 Hz actuation with 15% Ornstein–Uhlenbeck noise

of correlation (1/350) s versus 15% white noise of identical intensity. This exemplifies how correlated noise keeps the network exploring configuration space, while even with white noise it quickly sticks in a metastable state.

Changing the carrier frequency, rather than the added noise, controls the effective activity of the nodes leading to different positional distributions. Figure S6c,d gives histograms of the components c_1 and c_2 for actuation with carrier frequencies of 49 Hz (used in the main text Fig. 3) and 55 Hz plus 20% (1/345) s-correlated Ornstein–Uhlenbeck noise. The latter tightens in the stiff direction compared to the former, signifying greater ZM actuation relative to HMs, while the soft component changes shape more markedly as a result of the complex interactions of the network with the shaken baseboard.

* Present address: Mathematical Institute, University of Oxford, Andrew Wiles Building, Radcliffe Observatory Quarter, Woodstock Road, Oxford OX2 6GG, U.K.; Correspondence to: francis.woodhouse@maths.ox.ac.uk

[1] É. Fodor, C. Nardini, M. E. Cates, J. Tailleur, P. Visco, and F. van Wijland, Phys. Rev. Lett. **117**, 038103 (2016).
[2] P. Jung and P. Hänggi, Phys. Rev. A **35**, 4464 (1987).
[3] C. Maggi, U. M. B. Marconi, N. Gnan, and R. Di Leonardo, Sci. Rep. **5**, 10742 (2015).
[4] E. Jones, T. Oliphant, P. Peterson, *et al.*, "SciPy: Open source scientific tools for Python," (2001–), [http://www.scipy.org/].
[5] C. L. Kane and T. C. Lubensky, Nat. Phys. **10**, 39 (2014).
[6] C. J. Geyer, Stat. Sci. **7**, 473 (1992).
[7] T. J. Witt and N. E. Fletcher, Metrologia **47**, 616 (2010).
[8] D. B. Allan, T. Caswell, N. C. Keim, and C. M. van der Wel, "trackpy v0.4.1," (2018), [https://doi.org/10.5281/zenodo.1226458].